

Impact of Weak Lensing Mass Mapping Algorithms on Cosmology Inference

Andreas Tersenov^{1,2,3,*}, Lucie Baumont^{3,4,5}, Jean-Luc Starck^{2,3}, and Martin Kilbinger³

¹ Department of Physics, University of Crete, Greece

² Institutes of Computer Science and Astrophysics, Foundation for Research and Technology Hellas (FORTH), Greece

³ Université Paris-Saclay, Université Paris Cité, CEA, CNRS, AIM, 91191, Gif-sur-Yvette, France

⁴ Dipartimento di Fisica - Sezione di Astronomia, Università di Trieste, Via Tiepolo 11, 34131 Trieste, Italy

⁵ INAF-Osservatorio Astronomico di Trieste, Via G. B. Tiepolo 11, 34143 Trieste, Italy

Received; accepted

ABSTRACT

Context. Weak gravitational lensing is a powerful tool for probing the distribution of dark matter in the Universe. Mass mapping algorithms, which reconstruct the convergence field from galaxy shear measurements, play a crucial role in extracting higher-order statistics from weak lensing data to constrain cosmological parameters. However, only limited research has been done on whether the choice of mass mapping algorithm affects the inference of cosmological parameters from weak lensing higher-order statistics.

Aims. This study aims to evaluate the impact of different mass mapping algorithms on the inference of cosmological parameters measured with weak lensing peak counts.

Methods. We employ Kaiser-Squires, inpainting Kaiser-Squires, and MCALens mass mapping algorithms to reconstruct the convergence field from simulated weak lensing data, generated from cosmo-SLICS simulations. Using these maps, we compute the peak counts and wavelet peak counts as our data vectors. We perform Bayesian analysis with MCMC sampling to estimate posterior distributions of cosmological parameters, including matter density, amplitude of matter fluctuations, and dark energy equation of state parameter.

Results. Our results indicate that the choice of mass mapping algorithm significantly affects the constraints on cosmological parameters, with the MCALens method improving constraints by up to 157% compared to the standard Kaiser-Squires method. This improvement arises from MCALens's ability to better capture small-scale structures. In contrast, inpainting Kaiser-Squires yields constraints similar to Kaiser-Squires, indicating limited benefit from inpainting for cosmological parameter estimation with peaks.

Conclusions. The accuracy of mass mapping algorithms is critical for cosmological inference from weak lensing data. Advanced algorithms like MCALens, which offer superior reconstruction of the convergence field, can substantially enhance the precision of cosmological parameter estimates. These findings underscore the importance of selecting appropriate mass mapping techniques in weak lensing studies to fully exploit the potential of higher-order statistics for cosmological research.

Key words. statistical – gravitational lensing: weak – cosmology: large-scale structure of Universe

1. Introduction

Weak gravitational lensing, or the distortion of distant galaxy images due to intervening mass along the line of sight, is a powerful cosmological probe (Kilbinger 2015).

In the past decade, weak lensing surveys, namely the Kilo Degree Survey (KiDS; Kuijken et al. 2019), the Dark Energy Survey (DES; Flaugher 2005; DES Collaboration 2022), and the Hyper Suprime Camera Survey (HSC; Aihara et al. 2017), and the Ultraviolet Near Infrared Optical Northern Survey (UNIONS, Guinot et al. 2022; Li et al. 2024), have imaged large areas of the extra-galactic sky to study the nature of dark matter, dark energy, and the sum of neutrino masses. The launch of the *Euclid* satellite (Euclid Collaboration et al. 2024) heralds a new generation of so-called Stage-IV weak lensing surveys, which will soon include the Vera C. Rubin Legacy Survey of Space and Time (LSST; LSST Dark Energy Science Collaboration 2012), and the Nancy Grace Roman telescope (Spergel et al. 2015). These instruments will conduct weak lensing measurements over an unprecedented area and depth.

Weak lensing surveys extract cosmological information primarily by measuring two-point summary statistics: the two-point galaxy shear correlation function and its Fourier equivalent, the power spectrum. However, current and future surveys are probing small angular scales with increasing precision. At these scales, weak lensing measurements contain non-Gaussian information due to non-linear structure formation that two-point statistics fail to capture (Weinberg et al. 2013). This has motivated the development of new summary statistics, known as higher-order statistics (HOS), designed to exploit the non-Gaussian information encoded in the matter density field. Some examples include peak counts (Marian et al. 2009; Dietrich & Hartlap 2010; Lin & Kilbinger 2015a,b; Harnois-Déraps et al. 2021; Ayçoberry et al. 2023; Harnois-Déraps et al. 2024), Minkowski functionals (Mecke et al. 1994; Kratochvil et al. 2012; Grewal et al. 2022), Betti numbers (Feldbrugge et al. 2019; Parroni et al. 2021), scattering transform coefficients (Cheng et al. 2020; Cheng & Ménard 2021), three-point statistics and the bispectrum (Takada & Jain 2003, 2004; Semboloni et al. 2011; Fu et al. 2014), map-level inference (Porqueres et al. 2022; Boruah & Rozo 2024), and the starlet- ℓ_1 norm (Ajani et al. 2021, 2023). Euclid Collaboration et al. (2023) have performed fore-

* e-mail: atersenov@physics.uoc.gr

casts of ten different HOS with a unified framework and found that they all outperform two-point statistics in terms of constraining power on the cosmological matter density parameter, Ω_m , the amplitude of the matter power spectrum, σ_8 , and the dark energy equation of state parameter, w_0 . While forecasts show the very promising potential constraining power of HOS, additional studies are required to demonstrate that systematic measurement errors can be controlled for these observables in practice.

Several HOS are computed from the two-dimensional convergence, κ , which is not directly observable. Instead, κ must be reconstructed from galaxy shears, in a process called "mass-mapping". This reconstruction is an ill-posed inverse problem, first because of galaxy shape noise and second because of missing data from observational artifacts such as bright stars, cosmic rays, and CCD defects. As a result, the fidelity of map reconstruction differs depending on the method used; see e.g. Jeffrey et al. (2021).

In the literature, metrics to compare mass-mapping methods are typically based on the quality of the map reconstruction, with the implicit assumption that methods with a higher fidelity produce tighter cosmological contours. However, the effects of mass-mapping methods on cosmological parameters measured with HOS have not yet been fully quantified. Furthermore, Grewal et al. (2024) found that different choices in the inversion method alter cosmological contours in a Fisher-forecast analysis using Minkowski functionals.

In this work, we go a step further and measure the effect of different mass-mapping methods on cosmological constraints from peak counts in a full inference pipeline.

Here, we focus on the following mass mapping methods: Kaiser-Squires (KS; Kaiser & Squires 1993), inpainting Kaiser-Squires (iKS; Pires et al. 2009), and MCALens (Starck et al. 2021). KS is a linear method that is fast but implements no denoising, and does not account for missing data or boundary effects; iKS is an improvement upon KS that provides an iteratively applied inpainting scheme to reduce the effect of missing data. Finally, MCALens combines a sparsity-based method that captures non-Gaussian information on small scales with a Gaussian random field to replicate Gaussian behavior on large scales (Starck et al. 2021).

We examine the effects of the preceding inversion methods on peak counts and wavelet peak counts. These summary statistics offer several unique advantages. They are fast to compute and have been shown to break the degeneracy between the standard model and fifth forces in the dark sector (Peel et al. 2018). Wavelet peak counts keep the advantages of peak counts but carry additional constraining power. In Stage-IV survey forecasts, Ajani et al. (2020) find that multi-scale wavelet peak counts yield tighter parameter constraints than a power spectrum analysis. This method is in fact so powerful that adding a power spectrum analysis does not further improve constraints compared to wavelet peak counts alone. Moreover, wavelet peak counts conveniently exhibit a covariance matrix that is nearly diagonal.

The structure of this paper is as follows: in Sect. 2, we describe the SLICS simulations and their associated mock data, as developed in Harnois-Déraps et al. (2021), for use in our inference pipeline. We review the HOS that we measure (peaks, wavelet peaks) in Sect. 3, followed by a description of our cosmological inference pipeline in Sect. 4. We then compare the cosmological contours derived using each mass-mapping reconstruction in Sect. 5. Finally, we conclude the paper in Sect. 6.

2. Simulations

One method to compute a theoretical prediction of HOS as a function of cosmological parameters is to forward-model the HOS from cosmological simulations. In the following, we introduce the SLICS N -body simulations (Harnois-Déraps et al. 2019), and describe how they are used to construct mock galaxy catalogues of the DES Y1 footprint (Harnois-Déraps et al. 2021). We subsequently employ these mock galaxy catalogues to apply our mass-mapping algorithms and compute the HOS.

2.1. Cosmology Training Set

In this work, we use the version of cosmo-SLICS described in Harnois-Déraps et al. (2021). These simulations are designed for the HOS analysis of weak lensing data, covering points over a wide range of the $[\Omega_m, \sigma_8, h, w_0]$ parameter space, where h is the Hubble parameter. They sample this space at 25 w CDM points as well as one Λ CDM point, arranged in a Latin Hypercube. At each of these points, a pair of N -body simulations with $1,536^3$ particles in a $(505 h^{-1} \text{ Mpc})^3$ co-moving volume is run, providing 2D projections of the matter density field. The precise mass of each particle is determined by the simulation volume and matter density and, therefore, varies with h and Ω_m , covering the range from 1.42 to $7.63 \times 10^9 M_\odot$. The 2D projections are afterward organized into 10 (5 for each of the 2 random seeds) past light-cone density maps, $\delta_{2D}(\theta, z)$, with a field of view of 100 deg^2 at different redshifts z . Those maps are in turn used to obtain convergence and shear maps, $\kappa(\theta, z_s)$ and $\gamma(\theta, z_s)$, for a number of source redshifts z_s , as described in Section 2.3. The mean source redshift in each tomographic bin is $\langle z_s \rangle = 0.403, 0.560, 0.773, 0.984$.

2.2. Covariance Mocks

The covariance matrix, which expresses the sample variance of our HOS, is evaluated from the SLICS suite of simulations, described in Harnois-Déraps et al. (2018). This set is comprised of 124 fully independent N -body simulations, run at a fixed cosmology¹, but with different random phases in the initial conditions. The specifications of this set (volume, number of particles, resolution) are the same as those of the cosmology training set. We further increase the effective number of simulations by a factor of 10, by generating 10 different shape noise realizations for each of the 124 simulations. The covariance matrix is then computed from the 1,240 realizations of this Covariance Training Set.

2.3. Matching Survey Properties

Harnois-Déraps et al. (2021) adapted the SLICS simulations to the DES Y1 survey by overlaying the simulated light cones with the data in a way that the resulting mock surveys have the (κ, γ) values from the simulations at the positions and intrinsic ellipticities of the galaxies in the data. This was implemented by segmenting the DES Y1 catalogues into 19 tiles, each with a size of 100 deg^2 , and populating every simulated map with the galaxy samples from the corresponding tile. In particular, the positions of the individual observed galaxies were replicated in every simulated survey realization. Every simulated galaxy was assigned

¹ The cosmology of the Covariance Training Set adopts the parameters: $\Omega_m = 0.2905$, $\Omega_\Lambda = 0.7095$, $\sigma_8 = 0.826$, $h = 0.6898$, and $n_s = 0.969$.

a redshift by sampling from the redshift distribution $n(z)$ corresponding to its tomographic bin.

In summary, each simulated light cone from the *cosmology* and *covariance training sets* is replicated 19 times, and linked to a full survey realization. As a final product, for the *cosmology training set*, we have 10 mock galaxy catalogue realizations for each of the 19 tiles that cover the DES Y1 footprint, at each of the 25 w CDM cosmologies and the single Λ CDM cosmology. For the *covariance training set*, we have 124 fully independent mock galaxy catalogue realizations at the fixed cosmology, for each of the 19 tiles.

3. Higher-Order Statistics on Weak Lensing Mass Maps

3.1. Mass mapping

The weak-lensing mass mapping problem is the task of reconstructing the convergence field κ from the measured shear field γ . This is possible because κ and γ are not independent, and can both be expressed as second-order derivatives of the lensing potential ψ :

$$\kappa = \frac{1}{2}\nabla^2\psi, \quad \gamma_1 = \frac{1}{2}(\partial_1^2 - \partial_2^2)\psi, \quad \gamma_2 = \partial_1\partial_2\psi. \quad (1)$$

where γ_1 and γ_2 are the two orthogonal components of the shear.

Rewriting the above equations in Fourier space, under the flat-sky approximation, we obtain the relation between convergence and shear:

$$\tilde{\kappa}(\mathbf{k}) = \frac{k_1^2 - k_2^2}{k^2} \tilde{\gamma}_1(\mathbf{k}) + \frac{2k_1k_2}{k^2} \tilde{\gamma}_2(\mathbf{k}), \quad (2)$$

where \mathbf{k} is the wave vector in Fourier space. This estimator of the convergence field, however, is only optimal in the case of zero noise and no missing (or masked) data. Moreover, Eq. (2) is only defined for $\mathbf{k} \neq 0$, which means that the mean κ cannot be recovered from γ alone. This problem is known as *mass-sheet degeneracy*.

To address these issues, several mass-mapping algorithms have been proposed in the literature. These techniques are based on different assumptions and methods and have been shown to produce different results in terms of the fidelity of the reconstructed maps. In this work, we compare the performance of the following mass-mapping techniques: the Kaiser-Squires (KS) method, the iterative Kaiser-Squires with inpainting (iKS), and the MCALens method. We provide a detailed description of these methods in App. A.

The original KS method is a direct linear inversion of the shear field to the convergence field, using the relation Eq. (2). Since this method is very fast, it has been widely used in weak lensing studies (e.g., Aycoberry et al. 2023; Euclid Collaboration et al. 2023; Dutta et al. 2024; Jeffrey et al. 2025). However, its simplicity leads to strong artifacts in the reconstructed convergence due to boundary effects, creates leakage between the E- and B-modes of the convergence field, and is not optimal in the presence of noise. The iKS algorithm is a variation of the KS method that iteratively applies the KS inversion along with an inpainting scheme that reduces the effects of missing data. The inpainting scheme uses the MCA iterative thresholding algorithm, introduced in Starck et al. (2005b); Starck et al. (2005), to fill in the missing convergence field data. This algorithm has been shown to improve the reconstruction of the convergence field in the presence of masks. Finally, the MCALens

method is a non-linear mass-mapping algorithm that combines a Gaussian component to capture large-scale behavior and a non-Gaussian component, constructed with sparsity priors, to recover the strong peaks in the convergence field at small scales. As a non-linear method, MCALens is computationally more expensive, but it provides a more accurate reconstruction of the convergence field, especially at small scales, where the non-Gaussian features of the matter distribution are more pronounced (Starck et al. 2021).

While there has been recent development of deep machine learning methods for mass mapping, e.g. Jeffrey et al. (2020); Remy et al. (2023), here we focus on unsupervised methods and leave comparison with deep learning methods for future work. Supervised methods, while promising, introduce issues such as training dataset representativity (i.e., the generalization problem). Moreover, in terms of mean square error, deep learning techniques have been shown to achieve results similar to those of MCALens (Remy et al. 2023). Additionally, although all of the above methods can be applied to data on the sphere, we instead take the approach of tiling the sky into small regions where the flat-sky approximation holds to ease comparison with the SLICS simulations during parameter inference, which are given in Cartesian coordinates.

3.2. Higher-Order Statistics

In this section, we describe the HOS in our pipeline: peak counts and wavelet peak counts.

Weak lensing peaks are defined as local maxima of the convergence field; in particular, we define peaks as pixels with a value larger than that of their eight neighbours in the image. These peaks trace projected overdensities in the matter distribution, and thus often indicate the presence of massive cosmic structures, although the precise relation between peaks and halos is complex due to projection effects and potential noise-induced false detections (Sabyr et al. 2022).

Peak count analysis is performed by calculating the peak function, which represents the number of peaks in a convergence map or signal-to-noise map as a function of the peak height (the respective pixel value). In this work, we count the peaks in signal-to-noise maps, obtained by dividing the noisy convergence maps κ , convolved with a filter \mathcal{W}_θ , by its corresponding rms map, σ_n^{filt} :

$$S/N = \frac{\mathcal{W}_\theta * \kappa}{\sigma_n^{\text{filt}}}. \quad (3)$$

Here, $*$ denotes the convolution operator, and σ_n^{filt} is derived from the rms map r of κ by $\sigma_n^{\text{filt}} = \sqrt{\mathcal{W}_\theta^2 * r^2}$.

Filtering of the convergence maps is necessary to reduce noise, especially at smaller scales where noise is dominant, and to assist in the detection of peaks. For the filtering, we employed two different approaches: a mono-scale and a multi-scale filtering, corresponding to a single Gaussian and a set of starlet (wavelet) filters, respectively.

The mono-scale approach consists of simply convolving the convergence maps with a single Gaussian kernel of size θ . The kernel size is chosen as a compromise between the need to reduce the noise and the need to preserve the signal. The multi-scale peak count analysis is performed by employing a wavelet decomposition to the map, namely the isotropic undecimated wavelet transform, commonly referred to as the starlet transform (Starck et al. 2007). This transform enables one to extract the

information encoded in different spatial scales quickly and simultaneously by decomposing the convergence maps into a set of wavelet bands of different scales. Specifically, the starlet filter decomposes the original $N \times N$ convergence map κ into a sum of images with the same number of pixels at different resolution scales j :

$$\kappa(x, y) = \sum_{j=1}^{j_{\max}} w_j(x, y) + c_j(x, y), \quad (4)$$

where c_j is a coarse, very smoothed, version of the original map, and w_j are the wavelet bands representing the details of the original map at scale 2^j pixels, j_{\max} is the maximum scale considered, and $J = j_{\max} + 1$. An important advantage of this analysis over other multi-scale approaches is that each wavelet band covers a different frequency range, resulting in a nearly diagonal peak count covariance matrix (Lin & Kilbinger 2018; Ajani 2021), which does not occur, for example, in the application of a multi-scale Gaussian analysis on the convergence map. In this starlet multi-scale approach, the standard deviation of noise σ_n^{filt} must be assessed separately for each wavelet band. It has been shown (Starck et al. 2015) that for starlet-decomposed images, the standard deviation of the noise at scale j can be estimated from the standard deviation of the noise of the original image σ_1 and some coefficients σ_j^e that represent the behaviour of the noise in wavelet space, as $\sigma_j = \sigma_j^e \sigma_1$. The coefficients σ_j^e are equal to the standard deviation at scale j of the starlet transform of a normal distribution with a standard deviation of one.

4. Inference Pipeline

4.1. Shear Maps

The output of the simulations described in Sect. 2 is a set of galaxy catalogues, each containing the positions, redshifts, the simulated shear components of the galaxies, and the simulated convergence field. We first concatenate the four redshift bins into one, so that each catalogue contains galaxies of all redshifts. We then project the galaxy right ascension and declination to Cartesian coordinates (x, y) onto a grid with a pixel size of 1 arcmin. This results in 600×600 pixel maps. To create the mask, we construct a galaxy number density map by binning the galaxy positions into the pixel grid, ($\mathbf{M} = 0$ where there are no galaxies, $\mathbf{M} = 1$ where there are galaxies).

Next, we bin the simulated shear components in the pixel grid to create the shear maps, and generate noise maps for both shear components using

$$\sigma_n^2 = \frac{\langle \sigma_{\text{int}}^2 \rangle}{\sqrt{2} n_{\text{gal}}}, \quad (5)$$

where $\langle \sigma_{\text{int}}^2 \rangle = 0.44$ is the average global intrinsic ellipticity dispersion of the source galaxies, and n_{gal} is the number of galaxies in the pixel. Here, we do not assume a constant galaxy number density, but rather use the actual number of galaxies in each pixel, to create a more realistic noise map. This noise map is added to the shear maps to create the mock observed shear maps.

Some studies (e.g., Marques et al. 2024; Cheng et al. 2024), choose to apply some smoothing to the shear maps before the mass mapping inversion. Our approach primarily involves filtering the reconstructed mass maps with various filters before calculating the HOS (see Section 3.2). However, we also incorporate a preprocessing step where the shear maps are smoothed

using a Gaussian kernel with a small standard deviation of 0.4 arcmin. This additional shear smoothing aims to reduce edge effects in the mass maps, particularly in the KS method, caused by pixels with no shear information. As shown in Section 4.2, this smoothing slightly improves the reconstruction accuracy of certain mass maps. Since we subsequently convolve the reconstructed mass maps with larger filters, this initial smoothing is not expected to bias our results. Ultimately, we conducted our analysis with both smoothed and unsmoothed shear maps but we observed no significant difference in the resulting cosmological parameter estimation. Consequently, we report only the results obtained with shear smoothing in this paper.

4.2. Mass mapping

In order to create mass maps, we apply the KS, iKS, and MCALens methods to the noisy shear maps. For the iKS and MCALens methods, we use 50 iterations. We set the detection threshold for the peaks in MCALens to 5σ .

In Figure 1, we show the mass maps obtained using the KS, iKS, and MCALens methods from a single tile of the simulated footprint. The KS and iKS maps have been smoothed with a Gaussian kernel with a standard deviation of 2 arcmin, to render the structures more visible. Without smoothing, the KS and iKS maps are dominated by noise. The MCALens maps, however, are already noise-suppressed by the mass-mapping algorithm, so they do not require additional smoothing for visualization purposes.

The iKS map uses inpainting to fill in the missing data in the convergence field (see Sect. 3.1), effectively reducing the edge effects visible in the KS map. For reference, large masked regions are outlined in white in the plots of the reconstructed mass maps. Additionally, we see that the MCALens method removes the noise, while keeping the stronger peaks in the convergence field, as expected from the method.

Table 1 presents a quantitative comparison of the reconstructed mass maps generated using the KS, iKS, and MCALens methods. The comparison evaluates shear maps processed with or without Gaussian smoothing (standard deviation 0.4 arcmin). The reconstruction accuracy is measured using the root mean square error (RMSE) between the true convergence map, κ_{true} , and the reconstructed map, κ_{rec} , calculated as:

$$\text{RMSE} = \sqrt{\frac{1}{N_{\text{mask}}} \sum_i \mathbf{M}_i (\kappa_{\text{true},i} - \kappa_{\text{rec},i})^2}, \quad (6)$$

where i is the pixel index, N_{mask} is the total number of unmasked pixels (i.e., where $\mathbf{M}_i = 1$), and \mathbf{M} is the binary mask. As shown in the table, applying Gaussian smoothing to the shear maps reduces the RMSE for the KS and iKS methods, indicating improved reconstruction accuracy. However, shear smoothing has minimal effect on the MCALens method, which consistently outperforms the others by achieving the lowest RMSE.

4.3. Statistics calculation

Once the mass maps are generated, we calculated our HOS on S/N maps, derived from the mass maps, as described in Section 3.2. We calculate the peak counts and wavelet peak counts only in regions where $\mathbf{M} = 1$, for both inpainted and non-inpainted maps, as the inpainted parts do not contain real signal. For both analyses, the S/N maps are constructed using Eq. (3), and peaks are counted and binned into 20 linearly spaced bins over the range $-2 < S/N < 6$, following Ajani et al. (2020).

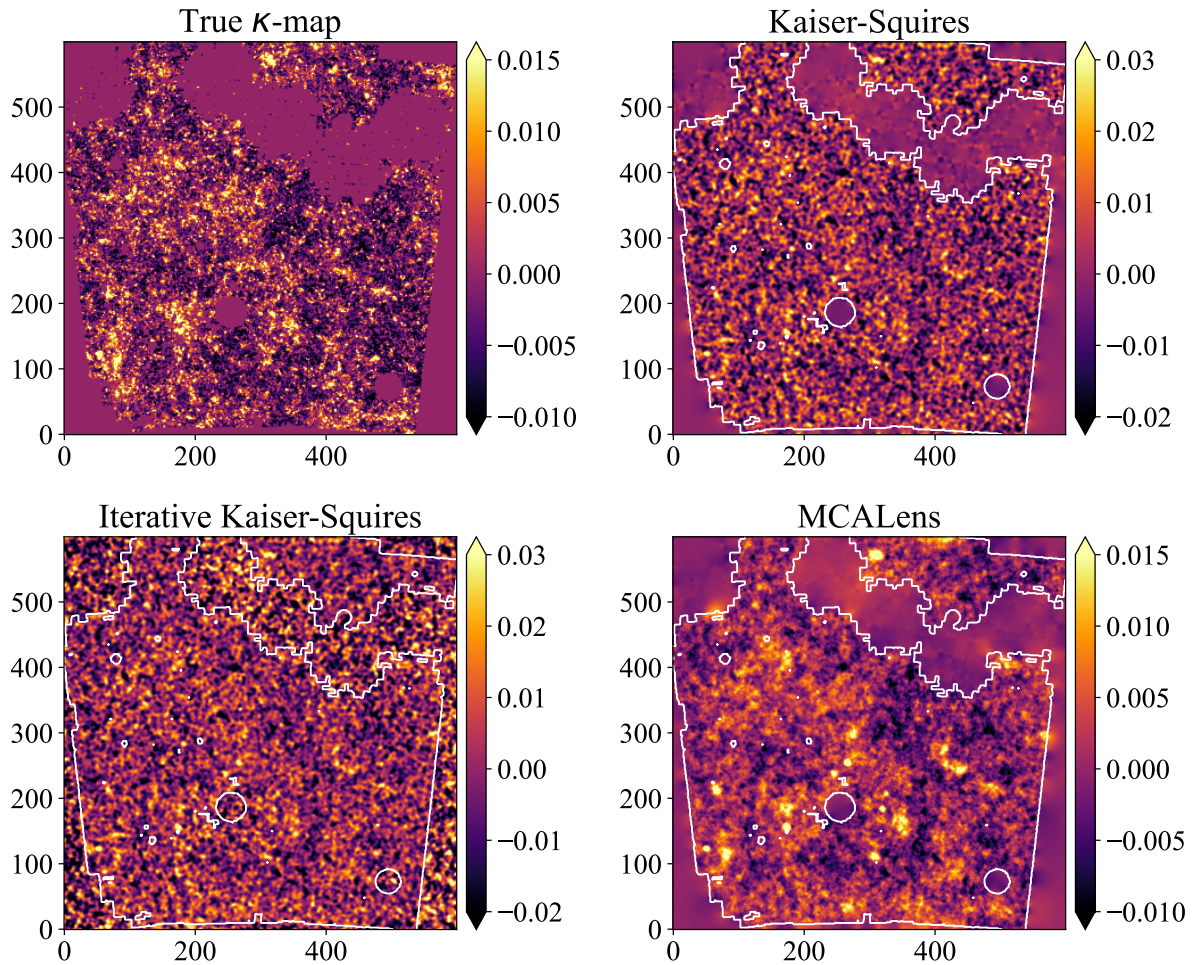


Fig. 1. Mass maps obtained using different reconstruction techniques, from a specific tile of the simulated footprint. The upper left panel displays the true convergence map derived directly from the simulated κ field. The upper right and lower left panels show the mass maps generated by the Kaiser-Squires (KS) and iterative Kaiser-Squires (iKS) methods, respectively, both smoothed with a Gaussian kernel (standard deviation of 2 arcmin) for visualization purposes. The lower right panel illustrates the MCALens mass map. The iKS method implements inpainting of the missing data, and the large masked regions of the patch are outlined in white.

Method	RMSE \downarrow
KS (no γ smoothing)	1.1×10^{-2}
iKS (no γ smoothing)	1.1×10^{-2}
KS (with γ smoothing)	1.0×10^{-2}
iKS (with γ smoothing)	1.0×10^{-2}
MCALens (no γ smoothing)	9.8×10^{-3}
MCALens (with γ smoothing)	9.8×10^{-3}

Table 1. Root mean square error (RMSE) comparison between the true convergence map and the reconstructed mass maps obtained using the KS, iKS, and MCALens methods. The RMSE is evaluated for mass maps derived from shear maps that are either smoothed with a Gaussian kernel of standard deviation 0.4 arcmin or left unsmoothed. The values represent the average RMSE across all realizations of the 25 cosmologies. To ensure a fair comparison, each mass map is further smoothed with a Gaussian kernel optimized to minimize its respective RMSE.

For the mono-scale peak counts, we use as the filter \mathcal{W} in Eq. (3) a Gaussian kernel. We tested various kernel sizes and selected the size that yielded the best cosmological constraints for

each method. The optimal kernel sizes were $\theta_{\text{ker}} = 2$ arcmin for the KS and iKS methods and $\theta_{\text{ker}} = 1$ arcmin for the MCALens method. We then count the peaks in the resulting S/N maps. Figure 2 displays the histograms of the peak counts for the KS, iKS, and MCALens methods, for the 25 simulated cosmologies. The histograms show the sensitivity of peak counts to cosmology as well as the difference between the mass-mapping methods.

For the wavelet peak counts, we first decomposed the convergence maps into wavelet scales using the starlet transform, as described in Sect. 3.2. We used five wavelet scales, which correspond to resolutions [2, 4, 8, 16, 32] arcmin, along with the coarse map. We then calculate the S/N maps for each wavelet band separately, according to Eq. (3) and count the peaks in each S/N map. Figure 3 shows the histograms of the wavelet peak counts for the KS, iKS, and MCALens methods, for the 25 simulated cosmologies. As expected, scales corresponding to smaller wavelet filters contain more peaks, as they capture smaller, more abundant structures in the convergence field. Notably, for most scales, MCALens results in a narrower distribution of peak counts, which is a result of the noise suppression by the method.

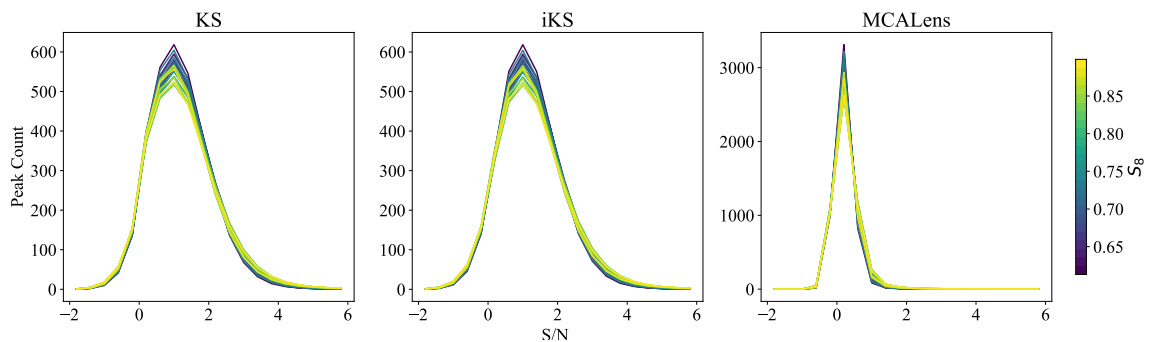


Fig. 2. Histograms of the peak counts as a function of the signal-to-noise ratio. The three panels from left to right correspond to the Kaiser-Squires (KS), iterative Kaiser-Squires (iKS), and MCALens methods, for the 25 simulated cosmologies. The histograms are colour-coded by their S_8 value.

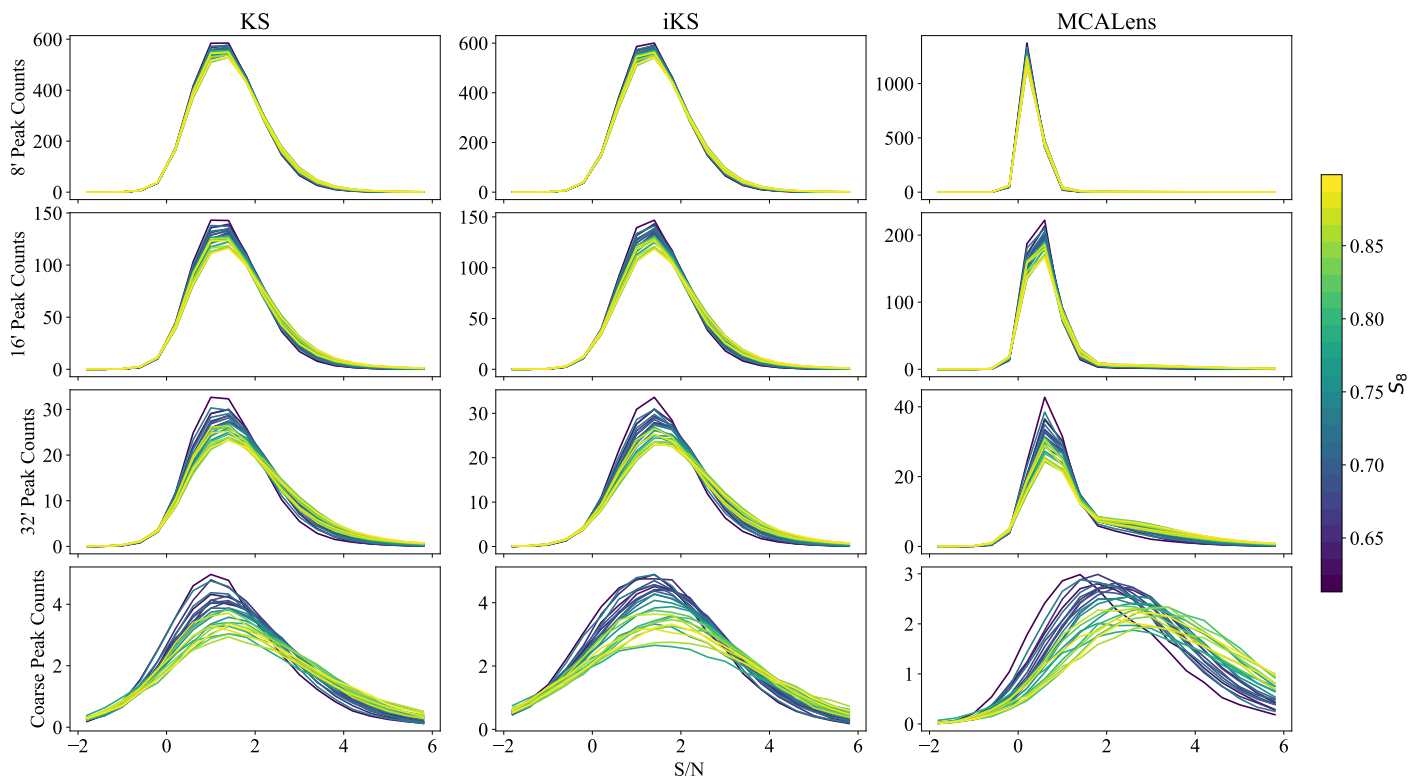


Fig. 3. Histograms of the wavelet peak counts as a function of the signal-to-noise ratio for the Kaiser-Squires (KS), iterative Kaiser-Squires (iKS), and MCALens methods, for the 25 simulated cosmologies. The four rows correspond to the three wavelet scales, [8, 16, 32] arcmin and the coarse map, and the columns correspond to the three mass mapping methods. The histograms are colour coded by their S_8 value.

4.4. Covariance matrices

We calculate the covariance matrices for the HOS, using the *Covariance Training Set* described in Section 4.4. To avoid unphysical large-scale mode-coupling that arises from replicating the same light-cone across tiles, we randomize the selection of light-cones during the survey construction, following Harnois-Déraps et al. (2021). For each of the 124 full survey realizations, we draw the 19 tiles from different, randomly selected light-cones. We apply this process to all 10 realizations and average them to create our final covariance matrix. The covariance matrix ele-

ments are calculated as:

$$C_{*,ij} = \sum_{r=1}^N \frac{(x_i^r - \bar{x}_i)(x_j^r - \bar{x}_j)}{N-1}, \quad (7)$$

where $N = 1240$ is the number of realizations in the *Covariance Training Set*, x_i^r is the value of the statistic in the i -th bin of the r -th realization, and \bar{x}_i is the mean of the i -th bin over all realizations:

$$\bar{x}_i = \frac{1}{N} \sum_{r=1}^N x_i^r. \quad (8)$$

We rescale the covariance matrices to account for the difference between the area of a single tile and the total survey area.

Each tile covers $10 \times 10 \text{ deg}^2$, and the survey footprint consists of 19 such tiles. To adjust for this, we divide each element of the covariance matrix by the ratio of the single-tile area to the total survey area. Moreover, to account for the finite number of bins and realizations, we use the de-biased estimator for an inverse Wishart distribution (Siskind 1972; Hartlap et al. 2007) for the inverse of the covariance matrix:

$$\mathbf{C}^{-1} = \frac{N - n_{\text{bins}} - 2}{N - 1} \mathbf{C}_*^{-1}, \quad (9)$$

where n_{bins} is the number of bins in the histogram of the HOS under consideration, and \mathbf{C}_*^{-1} is the inverse of the respective covariance matrix calculated according to Eq. (7).

In Fig. 4, we show the correlation matrices for the single-scale peak counts, for the different mass mapping methods. Figure 5 shows the correlation matrices for the wavelet peak counts.

4.5. Emulator

To obtain a prediction for our HOS for any given point in the parameter space $[\Omega_m, \sigma_8, h, w_0]$ within the range of our simulations, we construct an emulator using the Gaussian Process Regression (GPR) method². For each bin of the HOS histograms, we train a separate GPR model on all realizations of the HOS from the Cosmology Training Set. We found that training the GPR models on the full set of realizations, rather than just the mean HOS histograms, improved the emulator's performance. This approach enables the GPR models to predict the scaled HOS values in each histogram bin as a function of the cosmological parameters while simultaneously capturing the variability across realizations through a Gaussian likelihood.

The GPR training involves optimizing the model hyperparameters by maximizing the marginal log-likelihood using the Adam optimizer. We employ a Radial Basis Function kernel with Automatic Relevance Determination, allowing the model to learn different length scales for each cosmological parameter. To ensure stability and efficiency, the HOS values are rescaled by their mean value in each bin during training, and the scaling factors are recorded for subsequent use in predictions.

We then validate the emulator by performing a leave-one-out cross-validation, where we train the GPR on all but one of the 25 cosmologies in the Cosmology Training Set, and then predict the HOS for the left-out cosmology. We repeat this process for all the cosmologies in the Cosmology Training Set, and we calculate the percentage error between the predicted and the true HOS. Because the training is done on one less cosmology than the full set, the leave-one-out cross-validation provides an upper limit on the error of the emulator. In particular, the error is overestimated in the case that the left-out cosmology is on the edge of the training volume, since in this case the emulator has to extrapolate from the other training points, instead of interpolating. We find that overall the emulator has percentage errors of less than 5% for all the HOS, which is acceptable for our purposes.

However, as discussed in Harnois-Deraps et al. (2024), the small number of available cosmologies in the cosmo-SLICS simulations used for training the emulator can lead to significant biases in the posterior distributions of the cosmological parameters. To mitigate these biases arising from the Gaussian Process emulator altogether, following Davies et al. (2024), we used the emulator's prediction of HOS at the given fiducial cosmology as our mock "observed" data vector. This choice is also made for

² We use the GPyTorch (version 1.12) Python package (Gardner et al. 2018) to implement the GPR.

simplicity and presentation purposes, as it assures that the contours will be centred around the fiducial cosmology, making it easier to compare the constraining power of the HOS for the different mass mapping methods. To ensure that this choice does not significantly alter the results of the analysis, we also perform the inference analysis using a mock data vector calculated from a cosmo-SLICS simulation at the fiducial cosmology, but in a simpler setting where the GPR is more robust. The results of this analysis are presented in the Appendix B.

4.6. Likelihood

To perform Bayesian inference and to estimate the posterior distributions of the cosmological parameters, we model the likelihood function by assuming that our HOS follow a multivariate Gaussian distribution at each cosmology point in the parameter space:

$$\log \mathcal{L}(\boldsymbol{\theta}|\mathbf{d}) = -\frac{1}{2} (\mathbf{d} - \boldsymbol{\mu}(\boldsymbol{\theta}))^T \mathbf{C}^{-1} (\mathbf{d} - \boldsymbol{\mu}(\boldsymbol{\theta})) \quad (10)$$

where \mathbf{d} is the data vector of the HOS, $\boldsymbol{\mu}(\boldsymbol{\theta})$ is the vector of the predicted HOS from the emulator at the point $\boldsymbol{\theta}$ in the parameter space, and \mathbf{C} is the covariance matrix of the HOS.

4.7. MCMC and posterior distributions

We perform a Markov Chain Monte Carlo (MCMC) analysis employing the emcee³ Python package. We assume flat priors for the parameters $\Omega_m \in [0.1019, 0.5482]$, $\sigma_8 \in [0.4716, 1.3428]$, $h \in [0.6034, 0.8129]$, and $w_0 \in [-1.9866, -0.5223]$, which are the boundaries of the training volume. We use the Gaussian likelihood function in Eq. (10), and a model-independent covariance, as described in Section 4.4. To verify the convergence of the chains, we use the Gelman-Rubin diagnostics (Gelman & Rubin 1992).

5. Results

In this section we present the results of our inference analysis for the parameters Ω_m , σ_8 , h , and w_0 , using the pipeline described in the previous section. We show the parameter constraints, estimated from peak counts and wavelet peak counts, and we investigate the impact of the choice of the mass mapping method on these constraints.

5.1. Mono Scale Peak counts

Figure 6 shows the constraints obtained from single-scale peak counts for the KS, iKS, and MCALens methods. We observe a substantial difference in the constraints obtained from the different mass mapping methods, with the MCALens method providing the tightest constraints, followed by the KS and the iKS method.

We further quantify these results by calculating the Figure of Merit (FoM) for each pair of parameters, defined as:

$$\text{FoM} = (\det \tilde{F})^{1/n}, \quad (11)$$

where \tilde{F} is the marginalized Fisher matrix, estimated as the inverse of the covariance matrix among the parameters of interest,

³ <https://github.com/dfm/emcee>

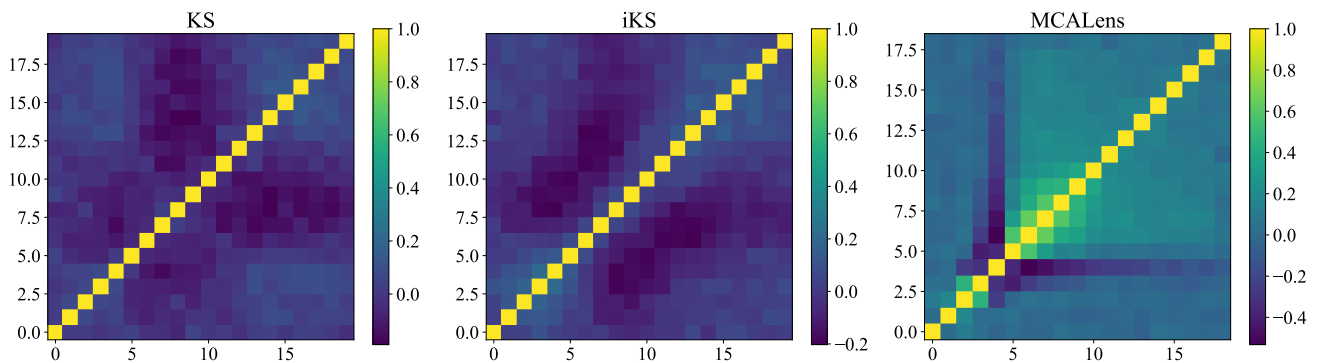


Fig. 4. Correlation matrices for the single-scale peak counts, for the Kaiser-Squires (KS), iterative Kaiser-Squires (iKS), and MCALens methods.

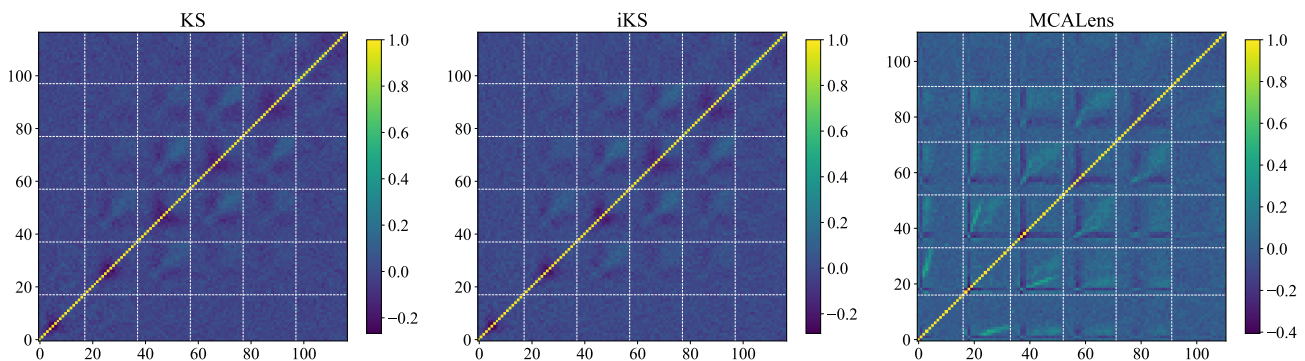


Fig. 5. Correlation matrices for the wavelet peak counts, for the Kaiser-Squires (KS), iterative Kaiser-Squires (iKS), and MCALens methods. The white dashed lines separate the different wavelet scales, which are positioned in increasing order of resolution from left to right, i.e. [2', 4', 8', 16', 32', coarse].

FoM	KS	iKS	MCALens
(Ω_m, h)	476	453	450
(Ω_m, w_0)	152	141	233
(Ω_m, σ_8)	1323	1285	1740
(h, w_0)	55	63	87
(h, σ_8)	336	292	293
(w_0, σ_8)	75	72	124
$(\Omega_m, h, w_0, \sigma_8)$	492	444	578

Table 2. Figure of Merit (FoM) for each pair of parameters, as well as for the full set of parameters, from the single-scale peak counts, for the Kaiser-Squires (KS), iterative Kaiser-Squires (iKS), and MCALens methods.

calculated from our MCMC chains, and n is the number of parameters. The FoM is a measure of the constraining power of the data on the parameters, with higher values indicating tighter constraints. Table 5.1 shows the FoM for each subset of parameters, as well as for the full set of parameters, for the KS, iKS, and MCALens methods. We can see that using MCALens instead of KS improves the FoM by 17%.

5.2. Wavelet peak counts

Figure 7 shows the constraints obtained from the wavelet peak counts, for the KS, iKS, and MCALens methods. As in the

case of the single-scale peak counts, we observe a clear difference in the constraints obtained from the different mass mapping methods, with the MCALens method delivering the tightest constraints, followed by the KS and the iKS method. Table 5.2 shows the FoM for each pair of parameters, as well as for the full set of parameters, for the KS, iKS, and MCALens methods.

As expected, the constraints produced from the wavelet peak counts are tighter than those from the single-scale peak counts, across all methods. However, the MCALens method shows a significantly greater relative improvement in the FoM when using wavelet peak counts, with a 157% enhancement compared to the KS method with wavelet peak counts. Furthermore, the combination of wavelet peak counts with the MCALens method enhances the FoM by 296% compared to single-scale peak counts with the KS method. These results underscore the critical importance of adopting a multiscale approach, both in the mass-map reconstruction and in the statistical analysis of the convergence field.

To assess the contribution of different wavelet scales across various methods, we also perform the inference analysis incrementally by including an increasing number of scales. We begin by obtaining constraints using the [16', 32', coarse] scales. Next, we successively add finer scales to this set, starting with the [8'] scale, followed by the [4'] scale, and, finally the [2'] scale.

The results are shown in Figs. 8 and 9 for the KS and MCALens methods, respectively. In Fig. 8, we observe that KS constraints improve significantly when including the [8'] scale, while the [4'] and [2'] scales do not provide significant additional

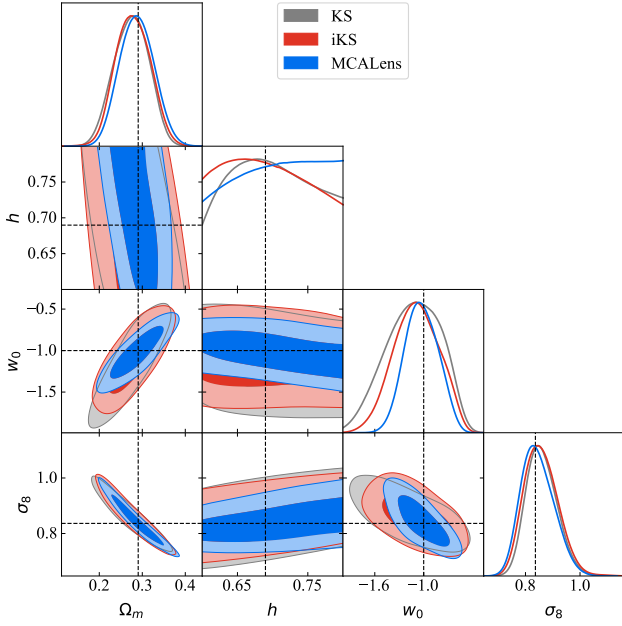


Fig. 6. Constraints on the parameters Ω_m , σ_8 , h , and w_0 from the single-scale peak counts, for the KS (gray), iKS (red), and MCALens (blue) methods. The contours represent the 68% and 95% confidence levels, and the black dashed lines indicate the true parameter values of our fiducial (Λ CDM) cosmology.

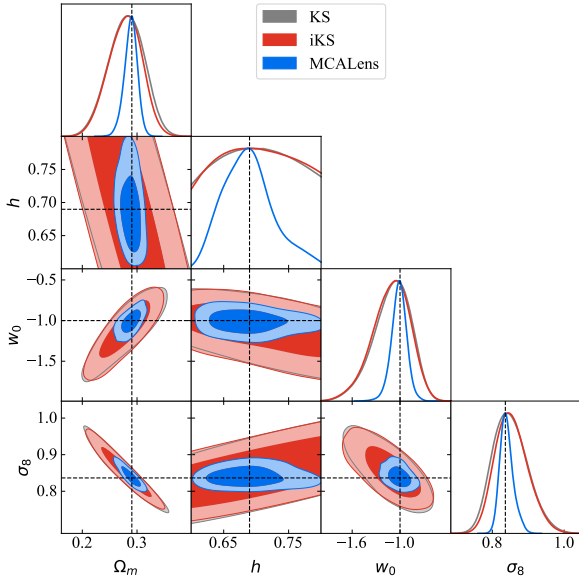


Fig. 7. Constraints on the parameters Ω_m , σ_8 , h , and w_0 from the wavelet peak counts with 6 wavelet scales [2', 4', 8', 16', 32', coarse], for the KS (gray), iKS (red), and MCALens (blue) methods. The contour lines are described in Fig. 6.

information. In contrast, Fig 9 shows that the MCALens constraints improve significantly with the inclusion of every smaller scale. This result highlights that the MCALens method is able to extract more information from the smaller scales of the convergence field, and that is where it gains most of its constraining power over the KS and iKS methods.

FoM	KS	iKS	MCALens
(Ω_m, h)	670	702	2159
(Ω_m, w_0)	247	244	1051
(Ω_m, σ_8)	2414	2517	9039
(h, w_0)	82	80	259
(h, σ_8)	411	433	1335
(w_0, σ_8)	131	129	577
$(\Omega_m, h, w_0, \sigma_8)$	758	755	1947

Table 3. Figure of Merit (FoM) for each pair of parameters, as well as for the full set of parameters, from the wavelet peak counts, for the Kaiser-Squires (KS), iterative Kaiser-Squires (iKS), and MCALens methods.

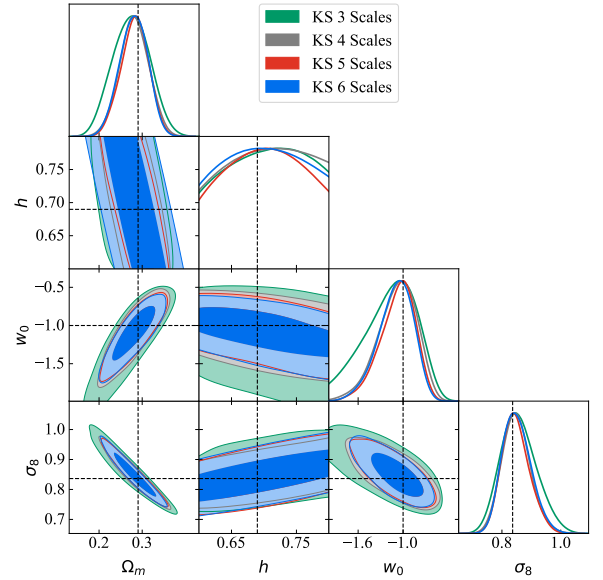


Fig. 8. Constraints on the parameters Ω_m , σ_8 , h , and w_0 from the wavelet peak counts using KS inversion and including different number of wavelet scales. The green contours were obtained with three scales: [16', 32', coarse], the gray contours were obtained by adding a fourth scale at 8'. The red contours were obtained by adding a fifth scale at 4', and the blue contours include a sixth scale at 2'. The contour lines are described in Fig. 6.

6. Conclusions

In this study, we investigated the impact of various mass mapping algorithms on cosmological inference using HOS derived from weak-lensing data. We have used a set of 25 simulated cosmologies to train an emulator for the HOS, and we have used a set of 1,240 realizations of the HOS for a fixed cosmology to estimate the covariance matrices. We have then performed a Bayesian analysis with an MCMC method to estimate the posterior distributions of the parameters Ω_m , σ_8 , h , and w_0 , using peak counts and wavelet peak counts as our data vectors. Our analysis shows that the choice of the mass mapping method has a significant impact on the constraints on the cosmological parameters, with the MCALens method providing the tightest constraints. The improvement by using MCALens is $\sim 17\%$ in the FoM compared to the KS method for the mono-scale analysis, and $\sim 157\%$ for the multi-scale analysis. We also find no significant difference in the contours created with the iKS and the

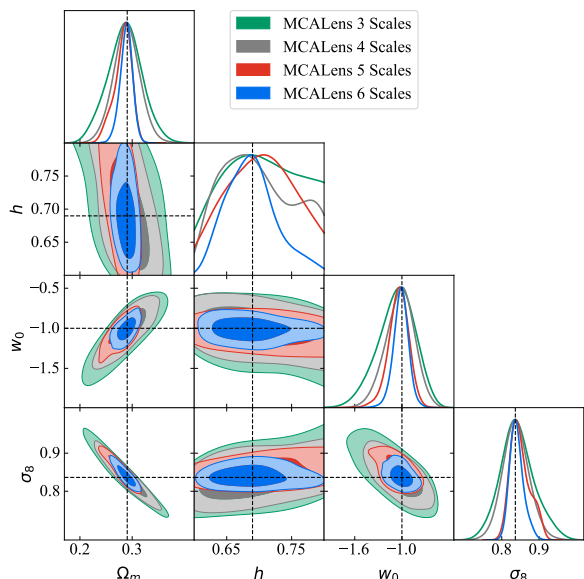


Fig. 9. Constraints on the parameters Ω_m , σ_8 , h , and w_0 from the wavelet peak counts using MCALens inversion including different number of wavelet scales. The green contours were obtained with three scales: [16', 32', coarse], and the gray contours were obtained by adding a fourth scale at 8'. The red contours were obtained by adding a fifth scale at 4', and the blue contours include a sixth scale at 2'. The contour lines are described in Fig. 6.

KS methods, indicating that forward modelling the inversion is sufficient to account for edge effects for both peak counts and multi-scale peak count statistics. Finally, we confirmed previous results that wavelet peak counts provide tighter constraints than single-scale peak counts. Constraints from MCALens increase the most by using a multi-scale approach because it captures additional information from smaller scales over KS.

These results highlight that a careful choice of mass mapping method to accurately reconstruct the convergence field can significantly improve constraints on the cosmological parameters from HOS.

Acknowledgements. This work was supported by the TITAN ERA Chair project (contract no. 101086741) within the Horizon Europe Framework Program of the European Commission, and the Agence Nationale de la Recherche (ANR-22-CE31-0014-01 TOSCA). LB is supported by the PRIN 2022 project EMC2 - Euclid Mission Cluster Cosmology: unlock the full cosmological utility of the Euclid photometric cluster catalog (code no. J53D23001620006). This work used the CANDIDE computer system at the IAP supported by grants from the PNCG, CNES, and the DIM-ACAV and maintained by S. Rouberol. The authors thank Nicolas Martinet, Virginia Ajani and Joachim Harnois-Déraps for useful discussions.

References

Aihara, H., Arimoto, N., Armstrong, R., et al. 2017, *Publications of the Astronomical Society of Japan*, 70, S4
Ajani, V. 2021, phdthesis, Université Paris Cité
Ajani, V., Harnois-Déraps, J., Pettorino, V., & Starck, J.-L. 2023, *Astronomy & Astrophysics*, 672, L10
Ajani, V., Peel, A., Pettorino, V., et al. 2020, *Physical Review D*, 102, 103531, publisher: American Physical Society
Ajani, V., Starck, J.-L., & Pettorino, V. 2021, *Astronomy & Astrophysics*, 645, L11
Ayçoberry, E., Ajani, V., Guinot, A., et al. 2023, *Astronomy & Astrophysics*, 671, A17, publisher: EDP Sciences

Bobin, J., Starck, J. L., Sureau, F., & Fadili, J. 2012, *Advances in Astronomy*, 2012, 703217, aDS Bibcode: 2012AdAst2012E..21B
Boruah, S. S. & Rozo, E. 2024, *MNRAS*, 527, L162
Cheng, S., Marques, G. A., Grandón, D., et al. 2024, arXiv preprint arXiv:2404.16085
Cheng, S. & Ménard, B. 2021, *MNRAS*, 507, 1012
Cheng, S., Ting, Y.-S., Ménard, B., & Bruna, J. 2020, *MNRAS*, 499, 5902
Davies, C. T., Harnois-Déraps, J., Li, B., et al. 2024, *Constraining modified gravity with weak lensing peaks*, arXiv:2406.11958 [astro-ph]
DES Collaboration. 2022, *Phys. Rev. D*, 105, 023520
Dietrich, J. P. & Hartlap, J. 2010, *MNRAS*, 402, 1049
Dutta, A., Peterson, J. R., Rose, T., et al. 2024, *ApJ*, 977, 87
Euclid Collaboration, Ajani, V., Baldi, M., et al. 2023, *A&A*, 675, A120
Euclid Collaboration, Mellier, Y., Abdurro'uf, et al. 2024, *Euclid. I. Overview of the Euclid mission*
Feldbrugge, J., van Engelen, M., van de Weygaert, R., Pranav, P., & Vegter, G. 2019, *J. Cosmology Astropart. Phys.*, 2019, 052
Flaugher, B. 2005, *International Journal of Modern Physics A*, 20, 3121
Fu, L., Kilbinger, M., Erben, T., et al. 2014, *MNRAS*, 441, 2725
Gardner, J. R., Pleiss, G., Bindel, D., Weinberger, K. Q., & Wilson, A. G. 2018, in *Advances in Neural Information Processing Systems*
Gelman, A. & Rubin, D. B. 1992, *Statistical Science*, 7, 457, publisher: Institute of Mathematical Statistics
Grewal, N., Zuntz, J., Tröster, T., & Amon, A. 2022, *The Open Journal of Astrophysics*, 5, 13
Grewal, N., Zuntz, J., & Tröster, T. 2024, *Comparing Mass Mapping Reconstruction Methods with Minkowski Functionals*, arXiv:2402.13912 [astro-ph]
Guinot, A., Kilbinger, M., Farrens, S., et al. 2022, *A&A*, 666, A162
Harnois-Déraps, J., Heydenreich, S., Giblin, B., et al. 2024, arXiv e-prints, arXiv:2405.10312
Harnois-Déraps, J., Amon, A., Choi, A., et al. 2018, *Monthly Notices of the Royal Astronomical Society*, 481, 1337
Harnois-Déraps, J., Giblin, B., & Joachimi, B. 2019, *Astronomy & Astrophysics*, 631, A160, publisher: EDP Sciences
Harnois-Déraps, J., Martinet, N., Castro, T., et al. 2021, *Monthly Notices of the Royal Astronomical Society*, 506, 1623
Hartlap, J., Simon, P., & Schneider, P. 2007, *Astronomy and Astrophysics*, 464, 399, aDS Bibcode: 2007A&A...464..399H
Heydenreich, S., Brück, B., & Harnois-Déraps, J. 2021, *Astronomy & Astrophysics*, 648, A74
Jeffrey, N., Gatti, M., Chang, C., et al. 2021, *MNRAS*, 505, 4626
Jeffrey, N., Lanusse, F., Lahav, O., & Starck, J.-L. 2020, *Monthly Notices of the Royal Astronomical Society*, 492, 5023
Jeffrey, N., Whiteway, L., Gatti, M., et al. 2025, *MNRAS*, 536, 1303
Kaiser, N. & Squires, G. 1993, *The Astrophysical Journal*, 404, 441, aDS Bibcode: 1993ApJ...404..441K
Kilbinger, M. 2015, *Reports on Progress in Physics*, 78, 086901, publisher: IOP Publishing
Kratohvil, J. M., Lim, E. A., Wang, S., et al. 2012, *Phys. Rev. D*, 85, 103513
Kuijken, K., Heymans, C., Dvornik, A., et al. 2019, *A&A*, 625, A2
Lanusse, F., Starck, J.-L., Leonard, A., & Pires, S. 2016, *Astronomy & Astrophysics*, 591, A2, publisher: EDP Sciences
Li, Q., Kilbinger, M., Luo, W., et al. 2024, *ApJ*, 969, L25
Lin, C.-A. & Kilbinger, M. 2015a, *A&A*, 576, A24
Lin, C.-A. & Kilbinger, M. 2015b, *A&A*, 583, A70
Lin, C.-A. & Kilbinger, M. 2018, *A&A*, 614, A36
LSST Dark Energy Science Collaboration. 2012, arXiv e-prints, arXiv:1211.0310
Marian, L., Smith, R. E., & Bernstein, G. M. 2009, *ApJ*, 698, L33
Marques, G. A., Liu, J., Shirasaki, M., et al. 2024, *Monthly Notices of the Royal Astronomical Society*, 528, 4513
Mecke, K. R., Buchert, T., & Wagner, H. 1994, *A&A*, 288, 697
Parroni, C., Tollet, É., Cardone, V. F., Maoli, R., & Scaramella, R. 2021, *A&A*, 645, A123
Peel, A., Pettorino, V., Giocoli, C., Starck, J.-L., & Baldi, M. 2018, *A&A*, 619, A38
Pires, S., Starck, J.-L., Amara, A., et al. 2009, *Monthly Notices of the Royal Astronomical Society*, 395, 1265
Porqueres, N., Heavens, A., Mortlock, D., & Lavaux, G. 2022, *MNRAS*, 509, 3194
Remy, B., Lanusse, F., Jeffrey, N., et al. 2023, *Astronomy & Astrophysics*, 672, A51
Sabyr, A., Haiman, Z., Matilla, J. M. Z., & Lu, T. 2022, *Phys. Rev. D*, 105, 023505
Semboloni, E., Schrabback, T., van Waerbeke, L., et al. 2011, *MNRAS*, 410, 143
Siskind, V. 1972, *Biometrika*, 59, 690
Spergel, D., Gehrels, N., Baltay, C., et al. 2015, arXiv e-prints, arXiv:1503.03757
Starck, J.-L., Elad, M., & Donoho, D. 2005a, *IEEE Transactions on Image Processing*, 14, 1570, conference Name: IEEE Transactions on Image Processing
Starck, J.-L., Fadili, J., & Murtagh, F. 2007, *ITIP*, 16, 297–309

- Starck, J.-L., Moudden, Y., Bobin, J., Elad, M., & Donoho, D. L. 2005b, in Wavelets XI, Vol. 5914 (SPIE), 209–223
- Starck, J. L., Moudden, Y., Bobin, J., Elad, M., & Donoho, D. L. 2005, in Society of Photo-Optical Instrumentation Engineers (SPIE) Conference Series, Vol. 5914, Wavelets XI, ed. M. Papadakis, A. F. Laine, & M. A. Unser, 209–223
- Starck, J.-L., Murtagh, F., & Fadili, J. 2015, Sparse Image and Signal Processing: Wavelets and Related Geometric Multiscale Analysis (Cambridge University Press)
- Starck, J.-L., Themelis, K. E., Jeffrey, N., Peel, A., & Lanusse, F. 2021, Astronomy & Astrophysics, 649, A99
- Takada, M. & Jain, B. 2003, MNRAS, 344, 857
- Takada, M. & Jain, B. 2004, MNRAS, 348, 897
- Weinberg, D. H., Mortonson, M. J., Eisenstein, D. J., et al. 2013, Phys. Rep., 530, 87

Appendix A: Mass mapping algorithms

Appendix A.1: Kaiser-Squires (KS)

In general, mass-mapping can be formulated as an inverse problem,

$$\gamma = \mathbf{A}\kappa + \mathbf{n}, \quad (\text{A.1})$$

where \mathbf{A} is the convolution matrix (which corresponds to the linear transformation from ideal κ -field to ideal γ -field), and \mathbf{n} is the noise vector. The matrix \mathbf{A} can be decomposed in Fourier space as $\mathbf{A} = \mathbf{F}\mathbf{P}\mathbf{F}^*$, where \mathbf{F} is the discrete Fourier transform matrix, and \mathbf{P} is the Fourier-space filter that relates the pure shear signal (in the absence of noise) to the convergence

$$\tilde{\gamma}_{\text{pure}} = \mathbf{P}\tilde{\kappa} = \left(\frac{k_1^2 - k_2^2}{k^2} + i \frac{2k_1k_2}{k^2} \right) \tilde{\kappa}. \quad (\text{A.2})$$

Here, $\tilde{\gamma} = \tilde{\gamma}_1 + i\tilde{\gamma}_2$ and $\tilde{\kappa} = \tilde{\kappa}_E + i\tilde{\kappa}_B$ are the complex representations of the two shear components and the convergence E and B -modes, in Fourier space, respectively.

The original method to solve the mass-mapping problem was proposed by Kaiser & Squires (1993).

This method directly inverts the relation between the observed shear γ and the convergence κ in Fourier space, as given by Eq. (2). In practice, this is done by directly applying the Fourier-space filter \mathbf{P}^{-1} to the shear field:

$$\tilde{\kappa} = \mathbf{P}^{-1}\tilde{\gamma} = \left(\frac{k_1^2 - k_2^2}{k^2} - i \frac{2k_1k_2}{k^2} \right) \tilde{\gamma}. \quad (\text{A.3})$$

While the KS method is the simplest and computationally fastest mass-mapping technique, it does not account for the noise, missing data, or the boundaries of the survey. This makes it suboptimal in the application to real data, leading to significant noise amplification, edge effects, and internal artifacts in the reconstructed maps, along with leakage between the E and B -modes of the convergence field. Typically, to reduce the noise in the reconstructed maps, some Gaussian smoothing is applied to the map. This, however, also leads to a loss of information at small scales and suppression of peaks.

To rigorously account for the noise covariance matrix Σ_n and the mask \mathbf{M} , we need to minimize the following Eq.:

$$\kappa_{ks} = \arg \min_{\kappa} \|\mathbf{M}(\gamma - \mathbf{A}\kappa)\|_{\Sigma_n}^2, \quad (\text{A.4})$$

which can be solved using the following iteration:

$$\kappa_{ks}^{n+1} = \kappa_{ks}^n + 2\mu \mathbf{A}^* \Sigma_n^{-1} (\mathbf{M}(\gamma - \mathbf{A}\kappa_{ks}^n)) \quad (\text{A.5})$$

where $\mu = \min(\Sigma_n)$. This iterative algorithm generalizes the standard KS solution, to take into account the noise covariance matrix and the mask. More details can be found in Starck et al. (2021), Appendix B.1.

Appendix A.2: Iterative Kaiser-Squires with DCT Inpainting (iKS)

Inpainting methods are techniques used to fill in missing data in an image or signal by estimating the missing values from known data. Sparse inpainting based on the Discrete Cosine Transform was proposed in Starck et al. (2005a,b) and used in the context of mass-mapping by Pires et al. (2009) to fill in areas of missing data in the convergence field.

Inpainting can be very easily included in Eq. A.4, so that one now minimizes the following equation:

$$\kappa_{iks} = \arg \min_{\kappa} \left\{ \|\mathbf{M}(\gamma - \mathbf{A}\kappa)\|_{\Sigma_n}^2 + \lambda \|\Phi^* \kappa\|_p \right\}, \quad (\text{A.6})$$

where $p = 0$ or 1 , Φ is the discrete cosine transform (DCT), and λ is a Lagrangian parameter. The solution can be obtained using the forward-backward algorithm:

– Forward step:

$$\mathbf{t} = \kappa_{iks}^n + 2\mu \mathbf{A}^* \Sigma_n^{-1} (\mathbf{M}(\gamma - \mathbf{A}\kappa_{iks}^n)) \quad (\text{A.7})$$

– Backward step:

$$\kappa_{iks}^{n+1} = \mathbf{M}\mathbf{t} + (1 - \mathbf{M})\Delta_{\Phi,\lambda}\mathbf{t} \quad (\text{A.8})$$

where $\Delta_{\Phi,\lambda}$ is the proximal operator defined in Pires et al. (2009), which consists of applying a DCT transform to u , thresholding the DCT coefficients, reconstructing an image from the thresholded coefficients, and normalizing the values of the filled-in pixels so that their standard deviation matches the standard deviation of the observed parts. This normalization can also be performed at every scale of the wavelet transform of the solution. Areas for which we possess information are processed as in the iterative KS case, while the inpainting regularisation affects areas with missing data (i.e. when $\mathbf{M} = 0$).

Appendix A.3: MCALens

MCALens method was developed in Starck et al. (2021) to combine the advantages of two different methods with complementary strengths: the Wiener filter and sparsity-based methods. The Wiener filter models the convergence field as a Gaussian random field. It effectively reconstructs the large-scale Gaussian features of the convergence field, but it is sub-optimal in reconstructing the small-scale features, such as peaks. On the other hand, methods based on sparsity priors, e.g. Lanusse et al. (2016), assume that the convergence field is sparse when represented in a certain basis. Sparsity-based methods excel in capturing these peak structures, but may struggle to retrieve the Gaussian-like statistical properties that emerge on larger scales.

To combine these two methods, MCALens models the convergence field as a sum of two components: a Gaussian component κ_G and a non-Gaussian component κ_S , sparse in a wavelet dictionary,

$$\kappa = \kappa_G + \kappa_S. \quad (\text{A.9})$$

MCALens then estimates κ_G and κ_S by applying the Morphological Component Analysis (MCA) algorithm, which is designed to separate different components mixed within a single signal or image, provided these components have distinct morphological properties. Specifically, MCA takes advantage of the sparsity of the different components in different dictionaries, which in the case of MCALens are a weighted Fourier basis for the Gaussian component,

$$\kappa_G = \Phi_G \alpha_G = \Sigma_{\kappa}^{-1/2} \alpha_G = \mathbf{P}_{\kappa}^{1/2} \mathbf{F} \alpha_G, \quad (\text{A.10})$$

and a wavelet basis for the sparse component,

$$\kappa_S = \Phi_S \alpha_S, \quad (\text{A.11})$$

The MCA algorithm is then solving the following optimization problem:

$$\min_{\kappa_G, \kappa_S} \left\{ \left\| \boldsymbol{\gamma} - \mathbf{A}(\kappa_G + \kappa_S) \right\|_{S_n}^2 + C_G(\kappa_G) + C_S(\kappa_S) \right\}, \quad (\text{A.12})$$

where C_G and C_S are regularization terms for the Gaussian and sparse components, respectively. The solution to this problem is found by iteratively applying the following steps:

1. Estimate κ_G by assuming that κ_S is known, minimizing:

$$\min_{\kappa_G} \left\{ \left\| (\boldsymbol{\gamma} - \mathbf{A}\kappa_S) - \mathbf{A}\kappa_G \right\|_{S_n}^2 + C_G(\kappa_G) \right\}. \quad (\text{A.13})$$

2. Estimate κ_S by assuming that κ_G is known, minimizing:

$$\min_{\kappa_S} \left\{ \left\| (\boldsymbol{\gamma} - \mathbf{A}\kappa_G) - \mathbf{A}\kappa_S \right\|_{S_n}^2 + C_S(\kappa_S) \right\}. \quad (\text{A.14})$$

To estimate the *Gaussian component*, the algorithm uses the Wiener filter, performing an iteration of the Proximal Wiener Filtering algorithm, as described in Starck et al. (2021), Section 2, at each MCA step. The Proximal Wiener Filtering is a variant of the standard Wiener filter (Bobin et al. 2012) which is designed to handle non-stationary noise, through the use of a Forward-Backward iterative algorithm. Thus, the penalty term C_G is in this case:

$$C_G(\kappa_G) = \|\kappa_G\|_{S_n}^2. \quad (\text{A.15})$$

For the *sparse component*, the algorithm cannot follow the typical ℓ_1 of ℓ_0 -norm regularization used in the standard sparse recovery algorithms, as the large-scale wavelet coefficients overlap with low-frequency Fourier coefficients of the Gaussian field, complicating their separation. Instead, the algorithm adopts an alternative two-step approach:

1. Identify the set of *active* wavelet coefficients by applying a threshold, typically 3-5 times the noise level at each scale j and position x . This results in a binary mask Ω , defined as:

$$\Omega_{j,x} = \begin{cases} 1 & \text{if wavelet coefficient} > \text{threshold,} \\ 0 & \text{otherwise} \end{cases}. \quad (\text{A.16})$$

The mask isolates the sparse features, distinguishing them from the Gaussian component.

2. Estimate the sparse component by solving the following minimization problem:

$$\min_{\kappa_S} \left\{ \left\| \Omega \odot \Phi_S^\dagger [(\boldsymbol{\gamma} - \mathbf{A}\kappa_G) - \mathbf{A}\kappa_S] \right\|_{S_n}^2 + C_S(\kappa_S) \right\}, \quad (\text{A.17})$$

where \odot denotes the element-wise multiplication, Φ_S^\dagger is the adjoint operator of the wavelet transform, and the penalty term C_S is given by:

$$C_S(\kappa_S) = i_{\mathbb{R}}(\kappa_S) \quad (\text{A.18})$$

where $i_{\mathbb{R}}$ is an indicator function to enforce real-valued solutions.

This approach offers the advantage that when Ω is fixed, the algorithm behaves almost linearly, with the only nonlinearity being the positivity constraint imposed on κ_S . This allows for the straightforward derivation of an approximate error map by simply propagating noise and relaxing the positivity constraint. The positivity constraint ensures that the reconstructed peaks are positive, which is not guaranteed in general, since peaks in the convergence field can be on top of voids and thus have negative values. The higher the non-Gaussianity of the convergence field, the more MCALens is expected to outperform linear methods like the Wiener filter.

Appendix B: Inference with simulated observations

In this appendix, we present the results of the inference analysis using as mock data the forward modelled HOS from the cosmo-SLICS simulations at the fiducial (Λ CDM) cosmology. The forward model applied to generate these fiducial data vectors is the same as the one used to generate the data vectors for the emulator training, described in Sections 4.1-4.3.

We then use the fiducial data vectors to estimate the size of the emulator's interpolation error that was not captured by our covariance matrix. To measure this, we train an additional GPR model on the mean values of the HOS histograms across realizations at the 25 cosmologies. From this model, we obtain the prediction uncertainties from the GPR at the fiducial cosmology. We then incorporate these interpolation errors into our error budget by adding them to the diagonal of the covariance matrix of the HOS data vectors, following Heydenreich et al. (2021).

The results for single-scale peak counts are shown in Fig. B.1. The constraints on the cosmological parameters are overall larger than those obtained using the emulator predictions as mock data, shown in Fig. 6, mainly due to the inclusion of the GPR interpolation error. Nevertheless, the contours still show that using MCALens instead of KS or iKS leads to significant improvements in the constraining power.

The results for wavelet peak counts are shown in Fig. B.2. These constraints were obtained using only 3 different scales: 16', 32', coarse. Including additional scales overly biased the GPR predictions due to the small number of cosmologies in the training set, leading to unreliable results. As in the case of single-scale peak counts, the resulting constraints are larger than those obtained using the emulator predictions as mock data, shown in Fig. 7 (both due to the use of only 3 scales, and the inclusion of the GPR interpolation error) but the improvement in the constraining power of MCALens over KS and iKS is still evident.

Regarding the bias in the cosmological parameters, the results show that the true values of the parameters are within the 68% confidence intervals for all mass-mapping methods and summary statistics. However, a more detailed analysis with a larger number of cosmologies in the training set would be necessary to draw more robust conclusions.

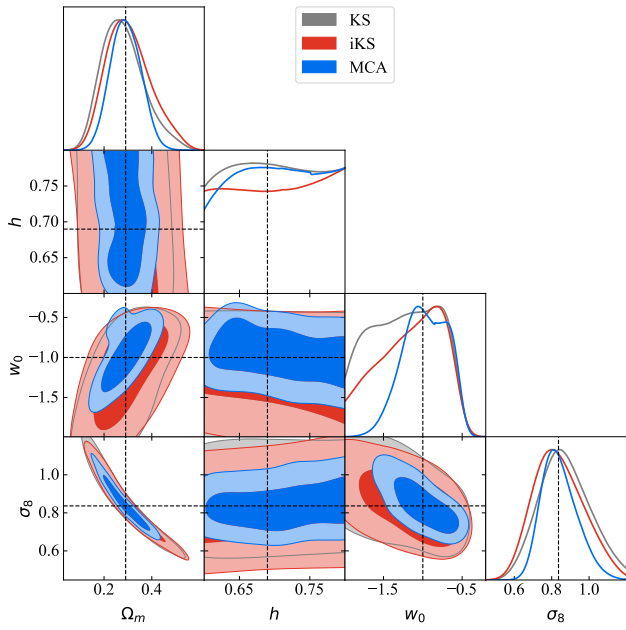


Fig. B.1. Constraints on the parameters Ω_m , σ_8 , h , and w_0 from single-scale peak counts, for simulated fiducial histograms. The contour lines are described in Fig. 6.

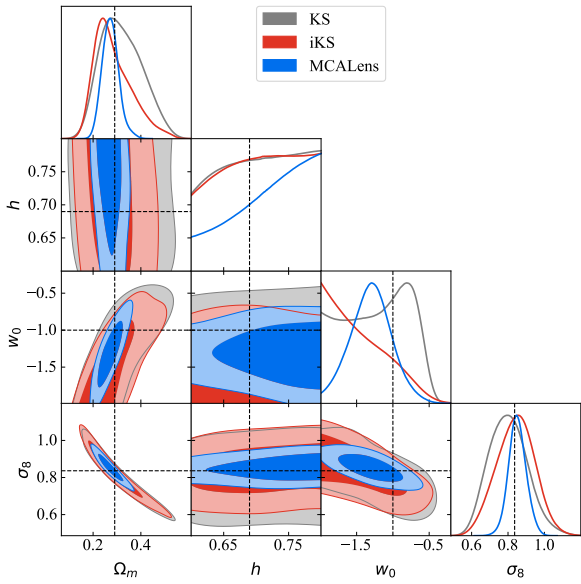


Fig. B.2. Constraints on the parameters Ω_m , σ_8 , h , and w_0 from wavelet peak counts with using the [16', 32', coarse] scales, for simulated fiducial histograms. The contour lines are described in Fig. 6.